Electronic Supplementary Information

Advanced Energy Harvesting from Low-Frequency Ocean Waves for Lithium-Ion Battery Applications

*Yingjin Luo,[a] Wentao Lei,[a] Pengfei Chen,[b] Tao Jiang,[b] Andeng Liu,[a] Meidan Ye,[a] Zijie Xu,[b] Zhong Lin Wang, *[b] and Wenxi Guo*[a]*

[a]Department of Physics, College of Physical Science and Technology, Research Institution for Biomimetics and Soft Matter, Xiamen University, Xiamen, Fujian, 361005 China. E-mail: wxguo@xmu.edu.cn

[b]Beijing Key Laboratory of Micro-Nano Energy and Sensor, Center for High-Entropy Energy and Systems, Beijing Institute of Nanoenergy and Nanosystems, Chinese Academy of Sciences, Beijing, 101400 P. R. China. E-mail: zhong.wang@mse.gatech.edu

† Electronic Supplementary Information (ESI) available. See DOI: 10.1039/x0xx00000x.

Supplementary Figures

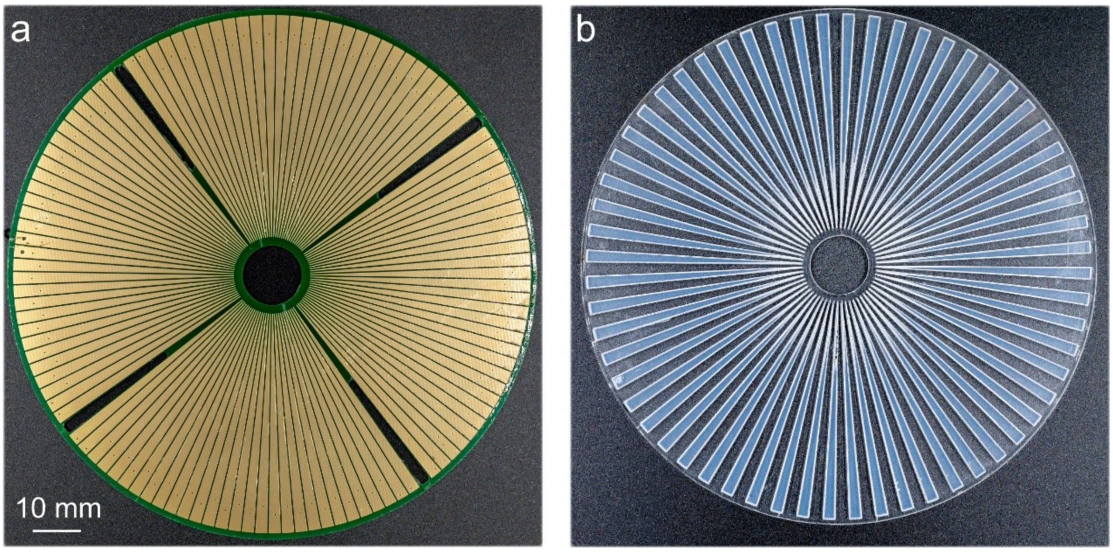

Fig. S1: Photograph of the stator and rotor. a. stator. b. rotor.

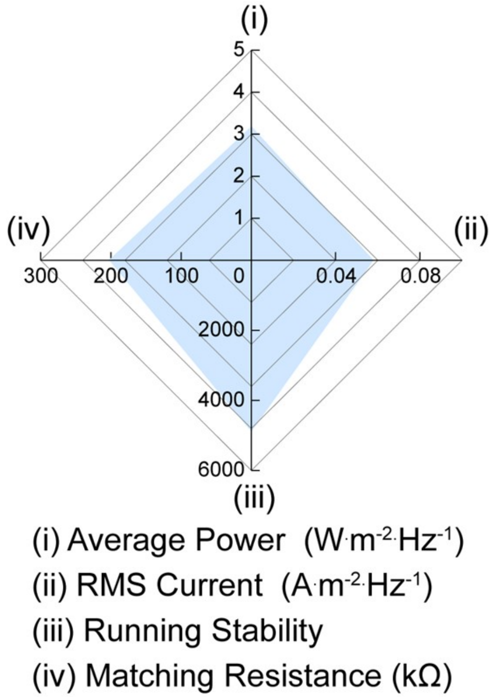

Fig. S2: Comprehensive evaluation of average power, RMS current, running stability and matching resistance for the RO-TENG.

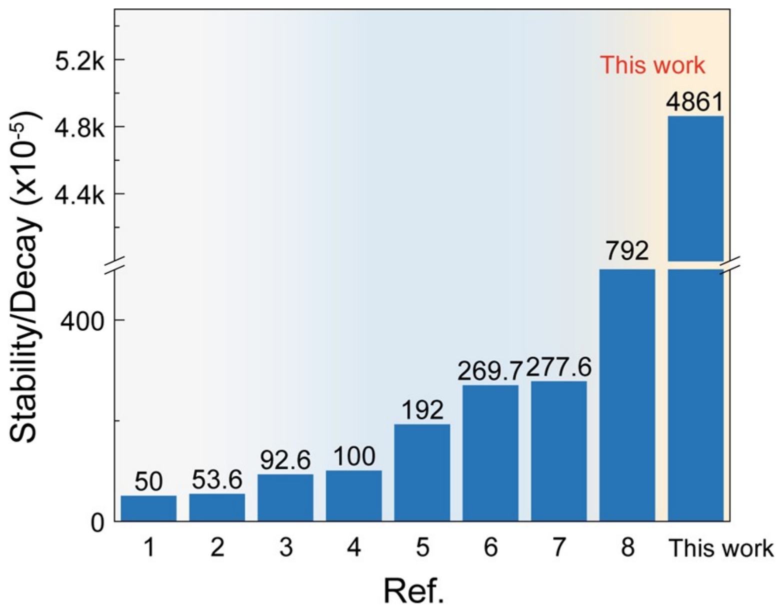

Fig. S3: Comparison of the stability of this work with others[1-8].

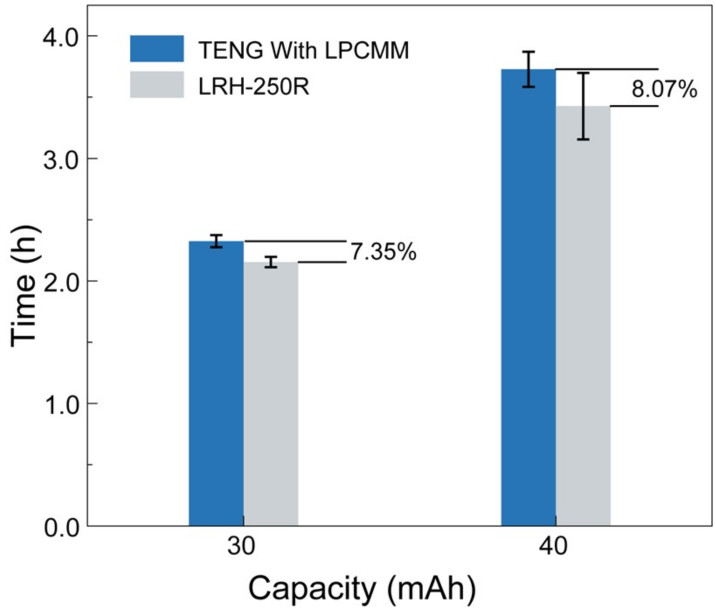

Fig. S4: A comparison of the time required to fully charge lithium batteries of various capacities using RO-TENG with LPCMM versus LRH-250R.

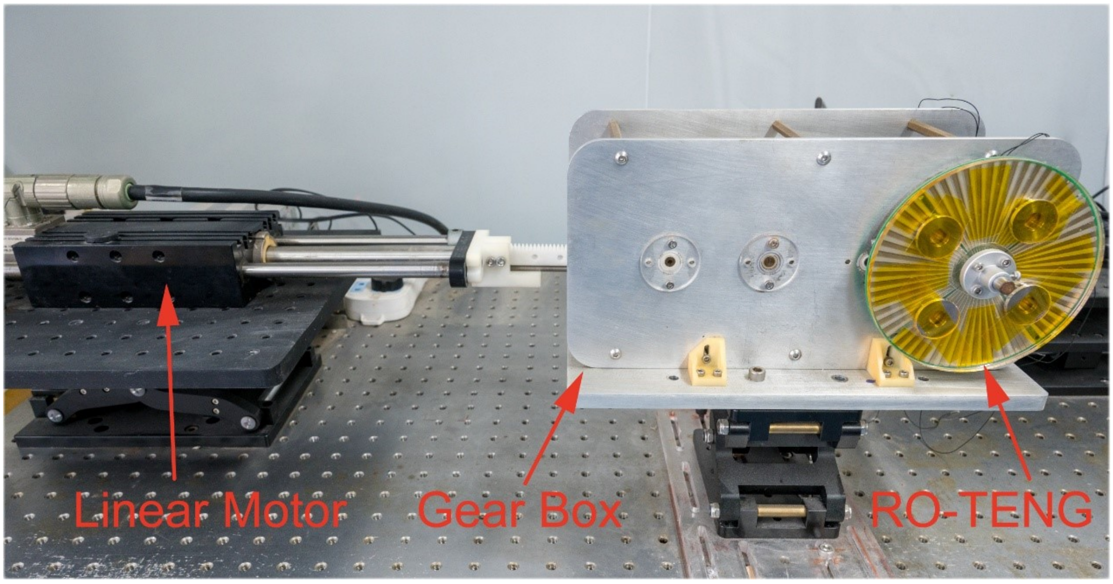

Fig. S5: Photograph of the linear motor test bench used for generating desired linear excitations.

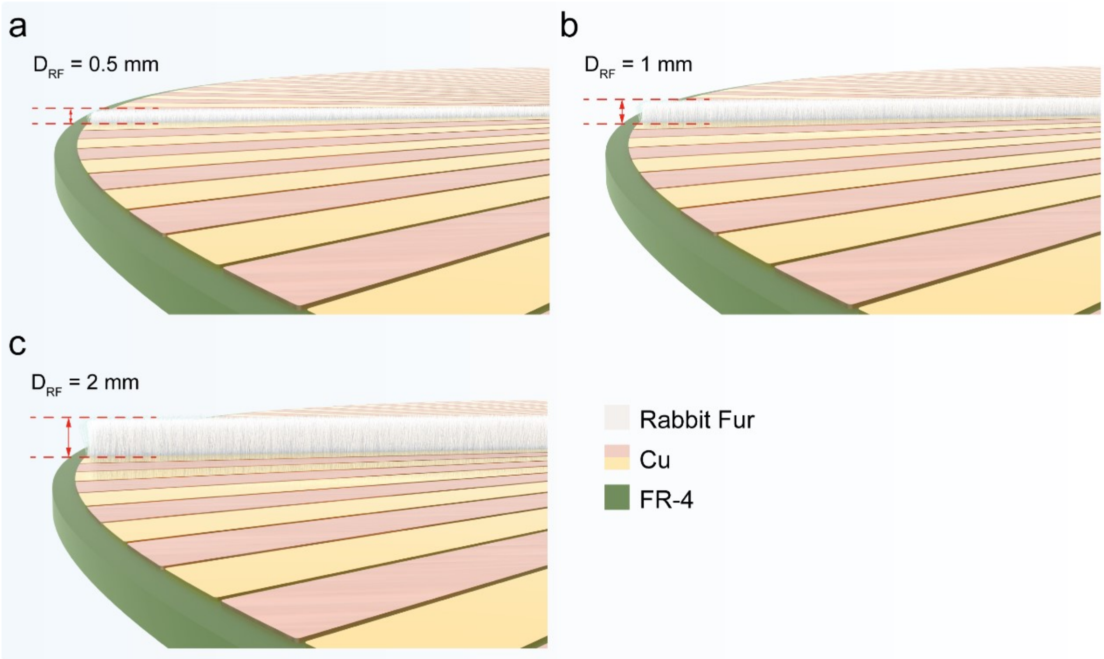

Fig. S6: Illustration of the distance between the rabbit fur to the stator surface (D_{RF}).

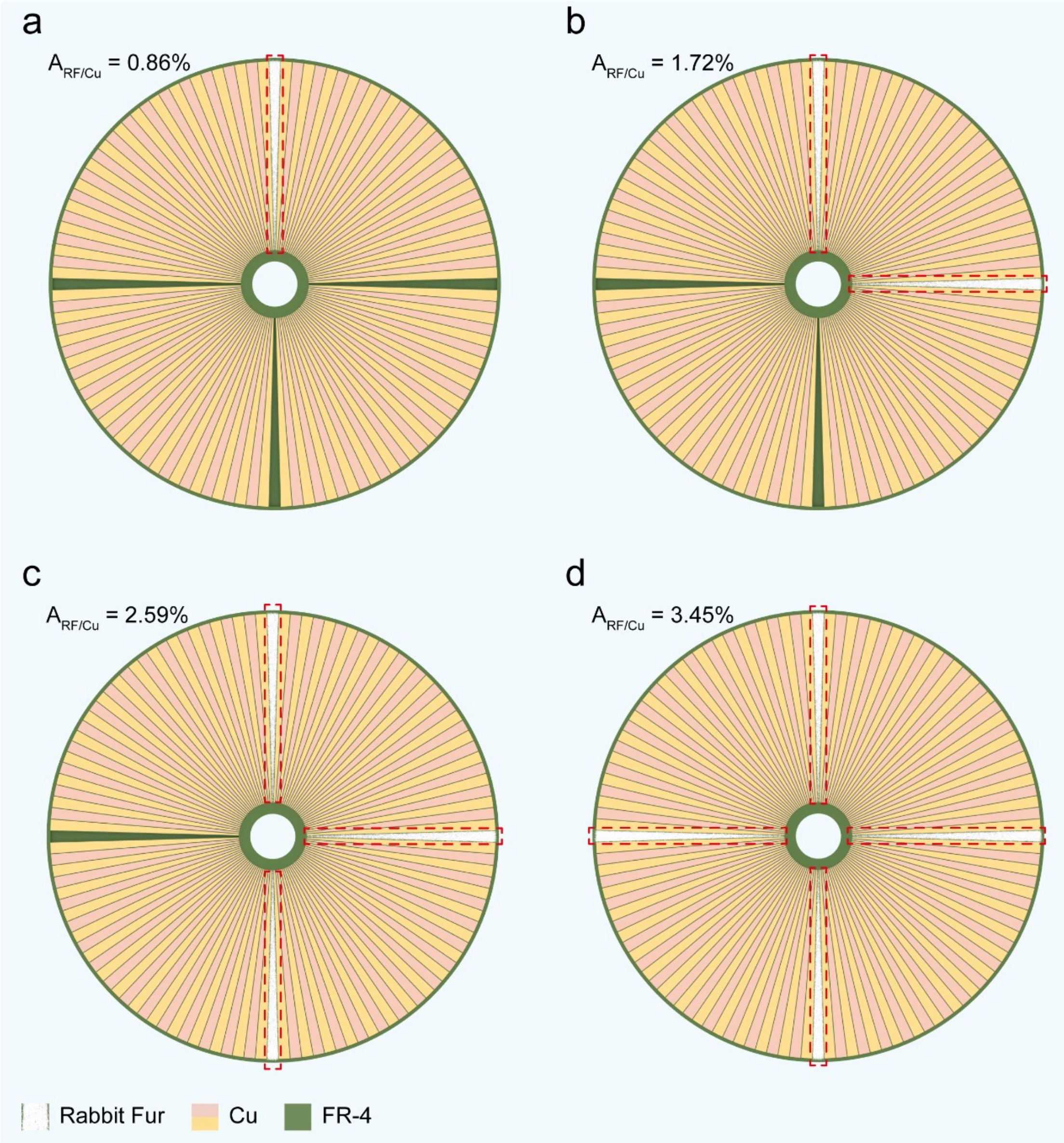

Fig. S7: Illustration of the specific ratio between the area of rabbit fur and the area of Cu electrode of the stator (the area of rabbit fur/the area of Cu electrode ($A_{RF/Cu}$)).

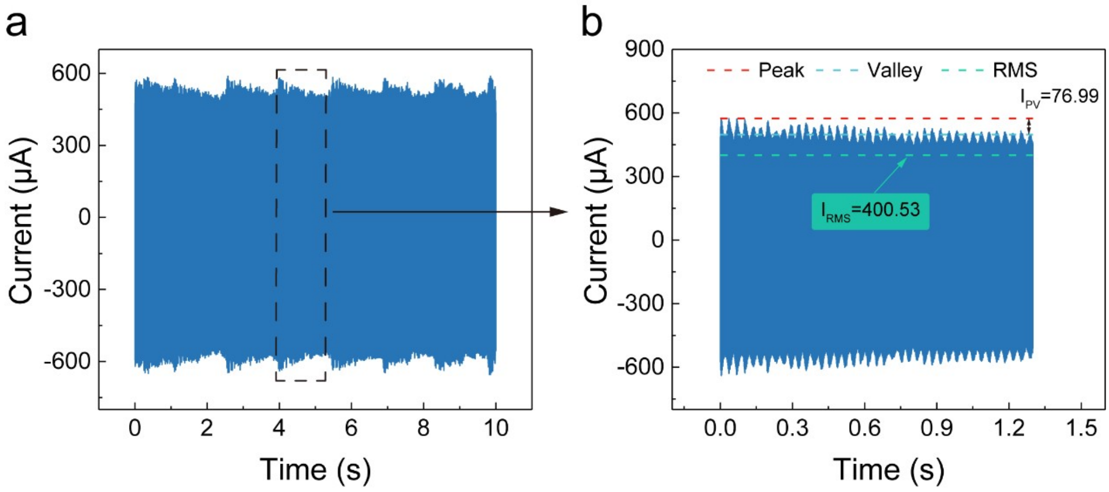

Fig. S8: a. Current data with $A_{RF/Cu} = 0$. b. Partial enlarged detail.

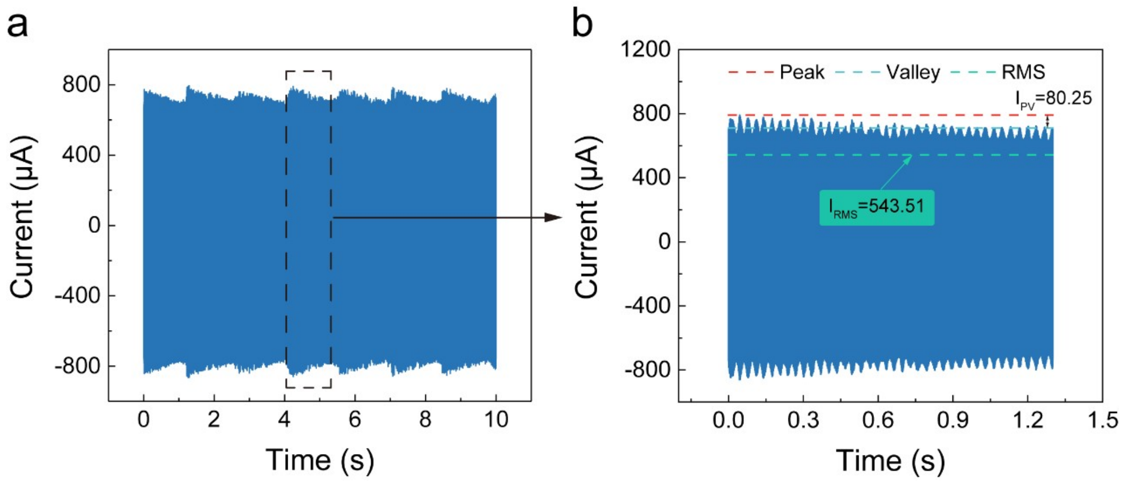

Fig. S9: a. Current data with $A_{RF/Cu}$ = 0.86%. b. Partial enlarged detail.

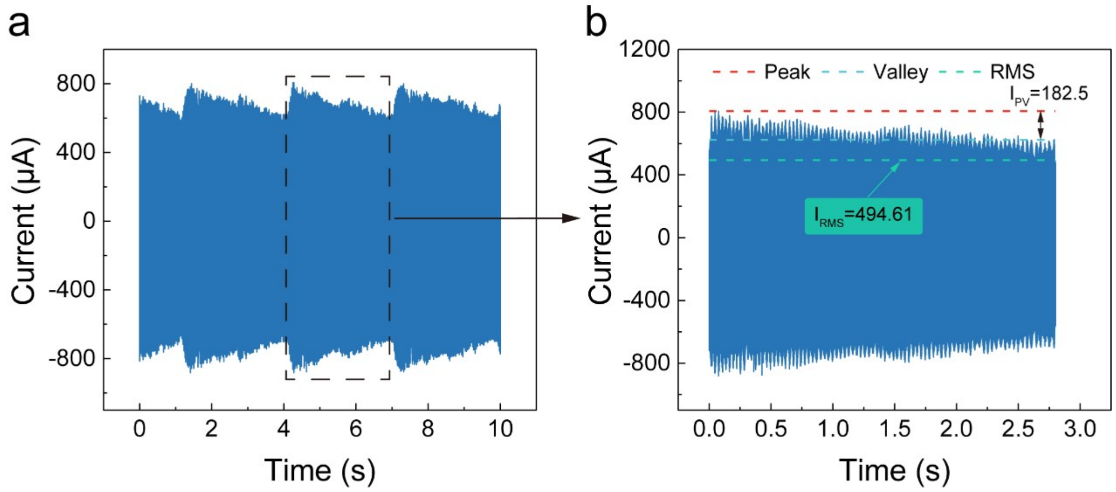

Fig. S10: a. Current data with $A_{RF/Cu}$ = 1.72%. b. Partial enlarged detail.

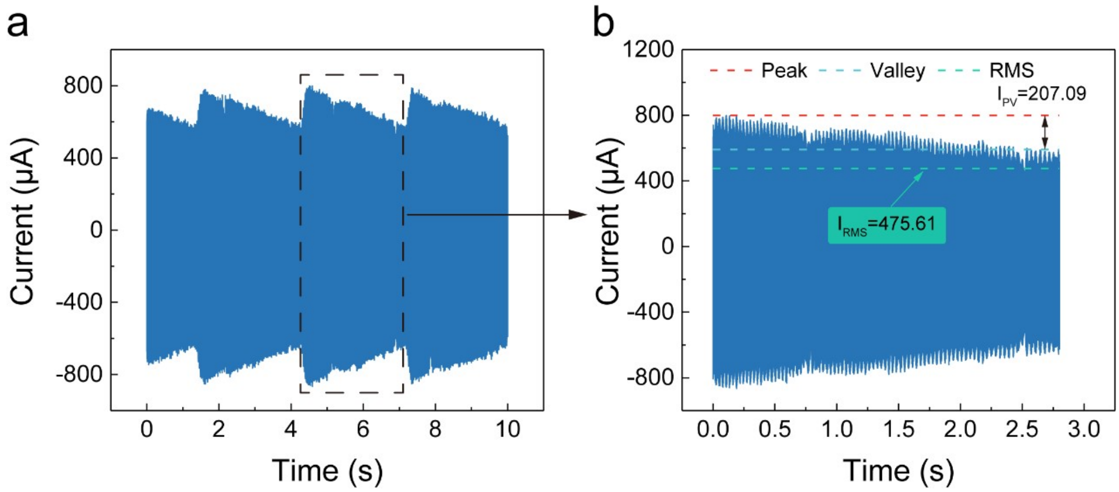

Fig. S11: a. Current data with $A_{RF/Cu}$ = 2.59%. b. Partial enlarged detail.

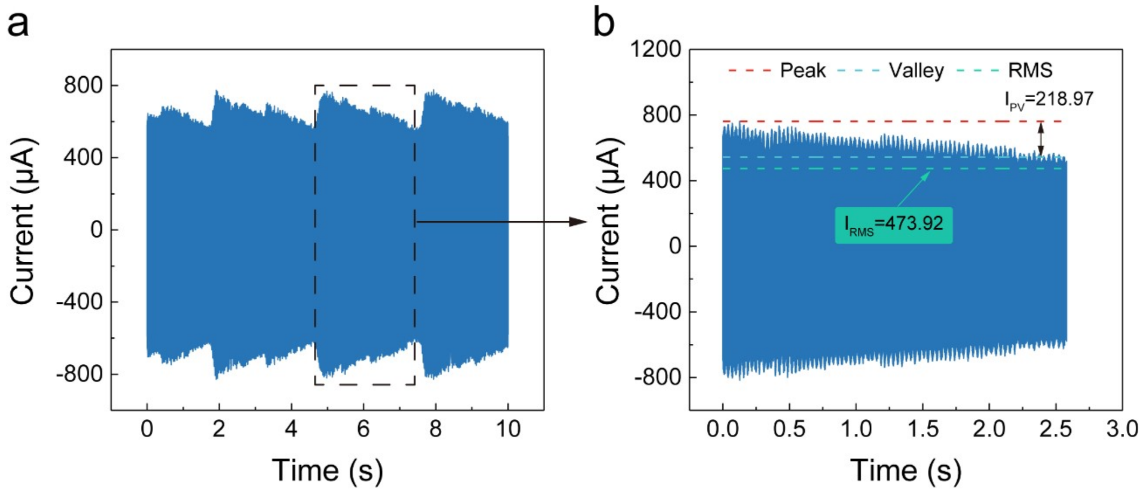

Fig. S12: a. Current data with $A_{RF/Cu}$ = 3.45%. b. Partial enlarged detail.

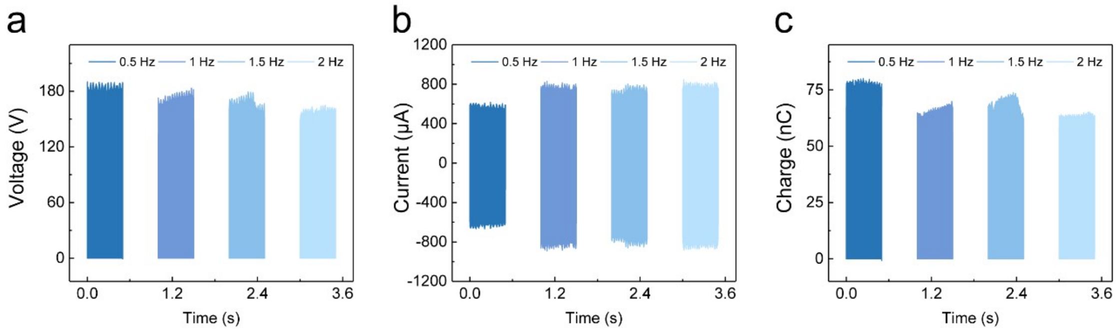

Fig. S13: Output performance of the RO-TENG with various frequency. a. Voltage data. b. Current data. c. Charge data.

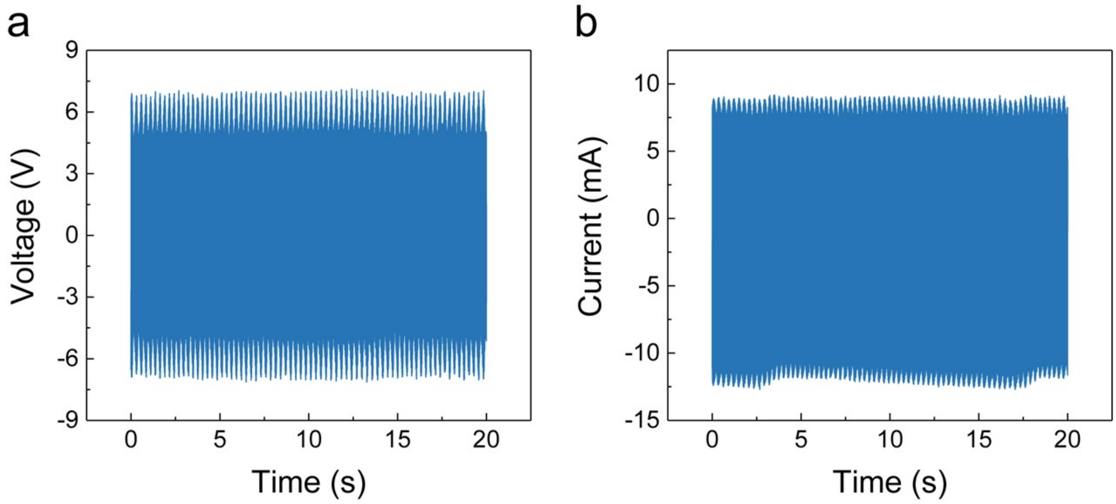

Fig. S14: Output performance of the RO-TENG with transformer. a. Voltage data. b. Current data.

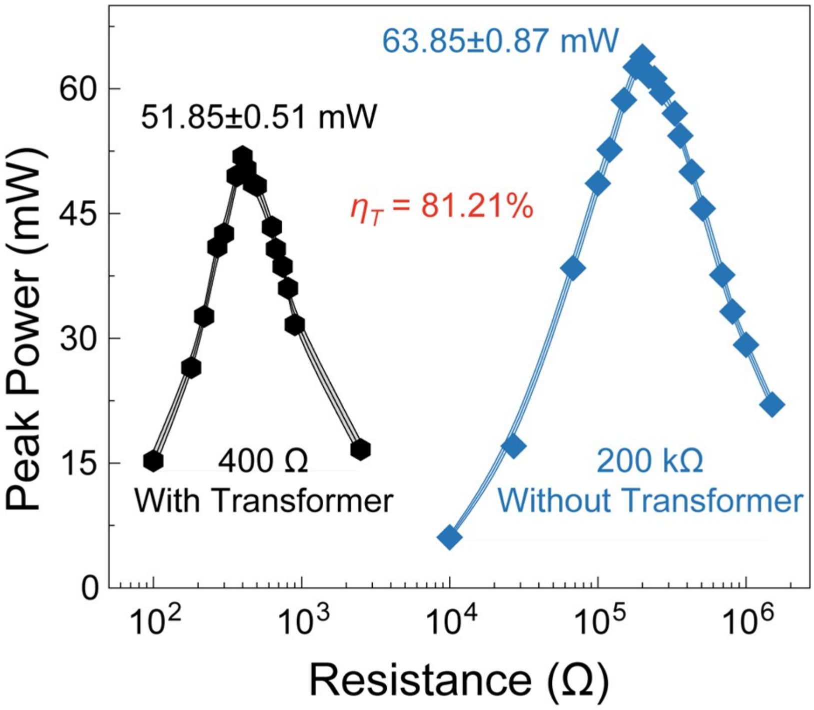

Fig. S15: Comparison of peak power between the cases with and without the transformer unit.

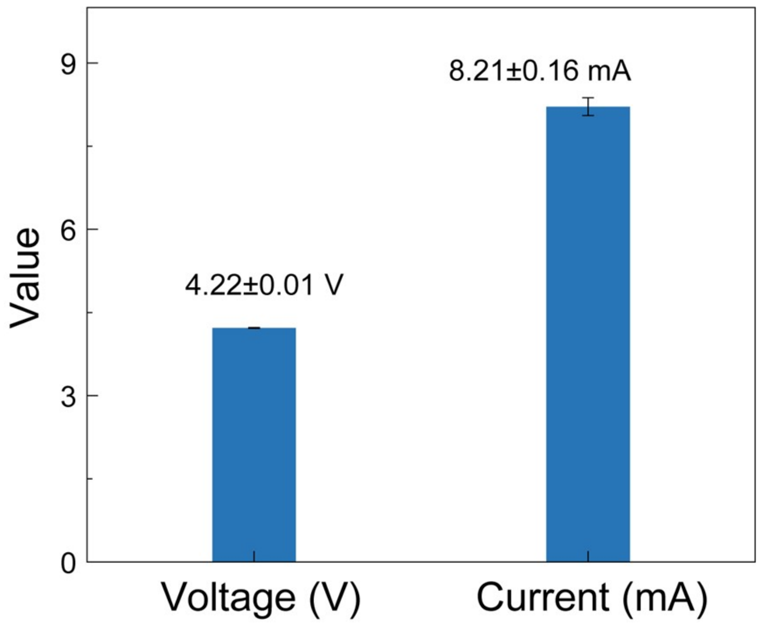

Fig. S16: Voltage and current data of the LPCMM with a single RO-TENG.

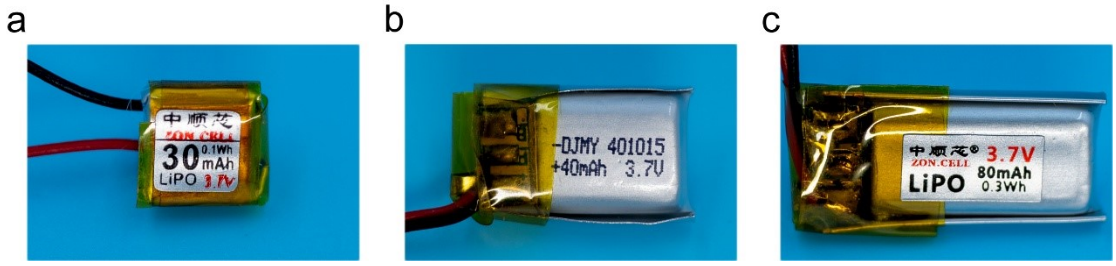

Fig. S17: Photograph of various capacity lithium batteries. a. 30 mAh lithium battery. b. 40 mAh lithium battery. c. 80 mAh lithium battery.

a b

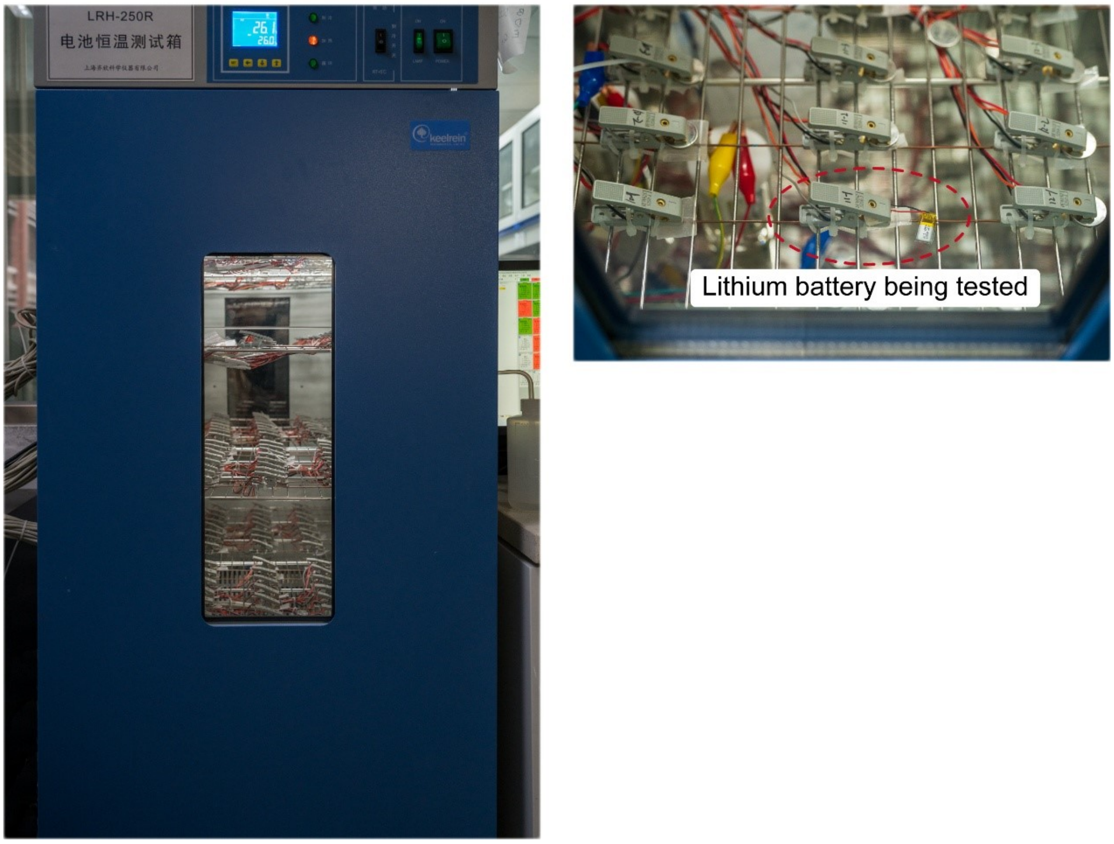

Fig. S18: a. Commercially available thermostatic lithium battery test systems (LRH-250R). b. Partial enlarged detail.

Manufacturer: Shanghai qixin scientific instrument Co., Ltd, China

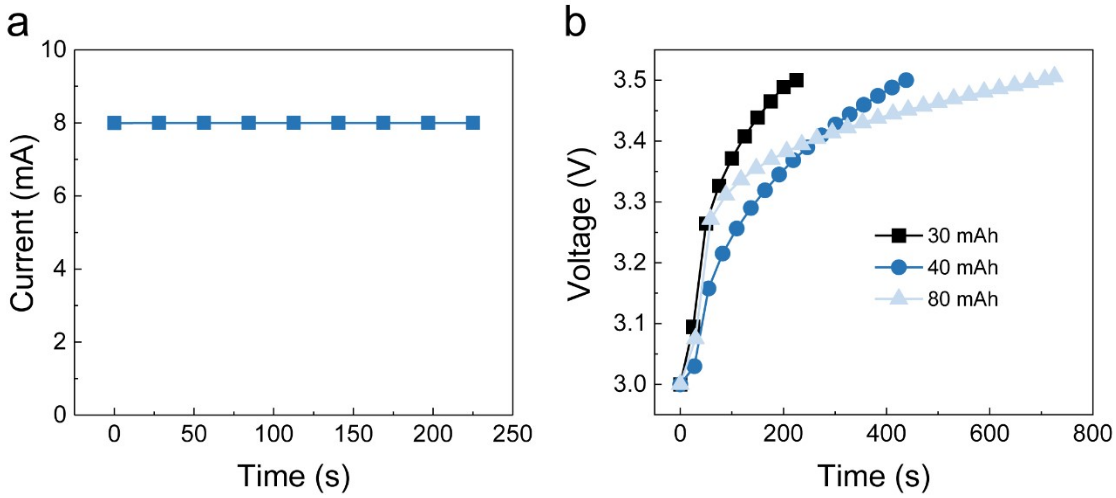

Fig. S19: a. Current data of the LRH-250R. b. Voltage curves for different capacities of lithium batteries powered by the LRH-250R at a charge current of 8 mA.

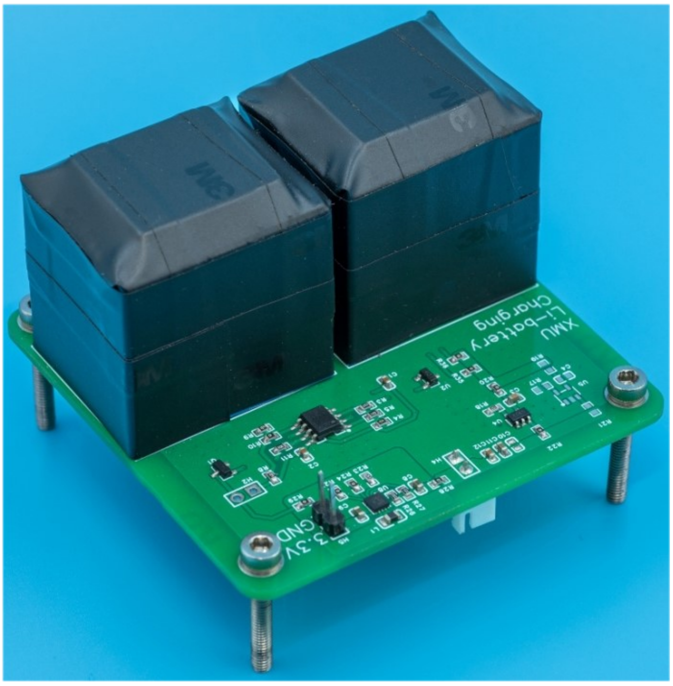

Fig. S20: Photograph of the two-input LPCMM.

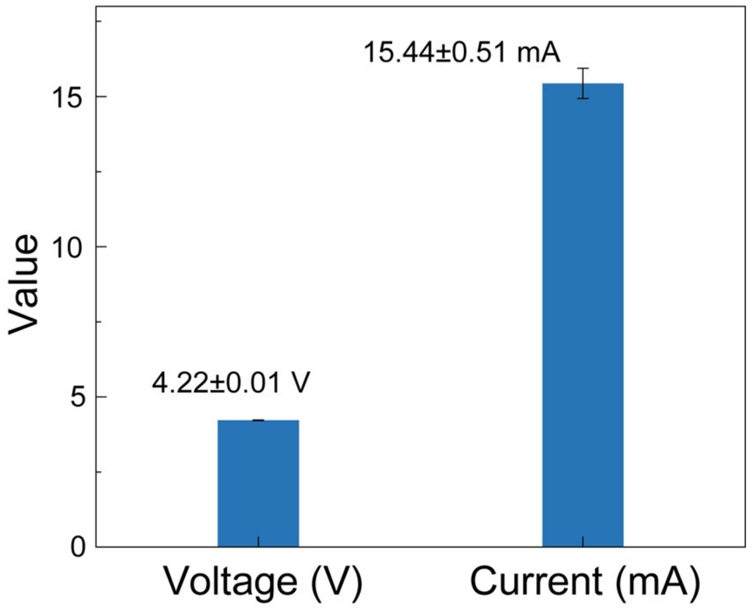

Fig. S21: Voltage and Current of the LPCMM with a parallel RO-TENG.

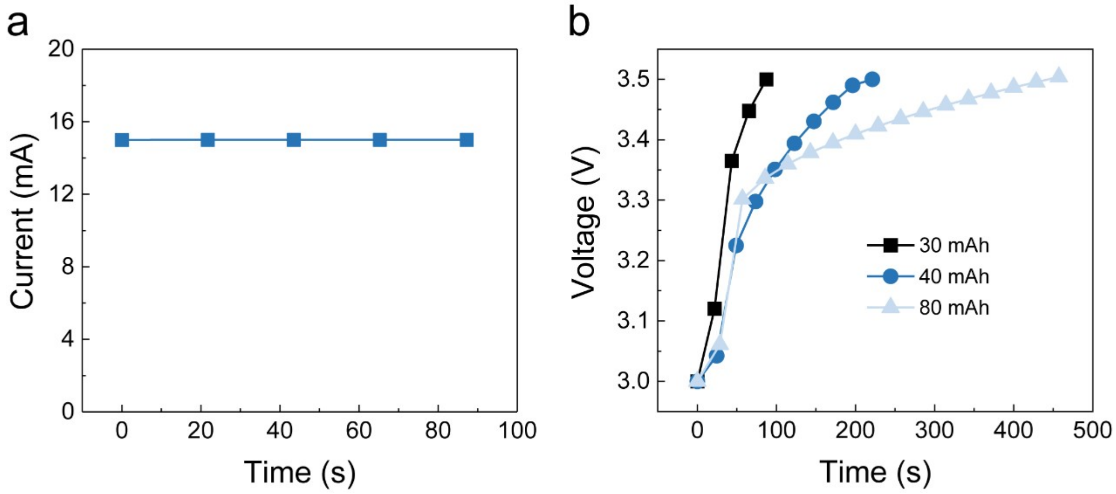

Fig. S22: a. Current data of the LRH-250R. b. Voltage curves for different capacities of lithium batteries powered by the LRH-250R at a charge current of 15 mA.

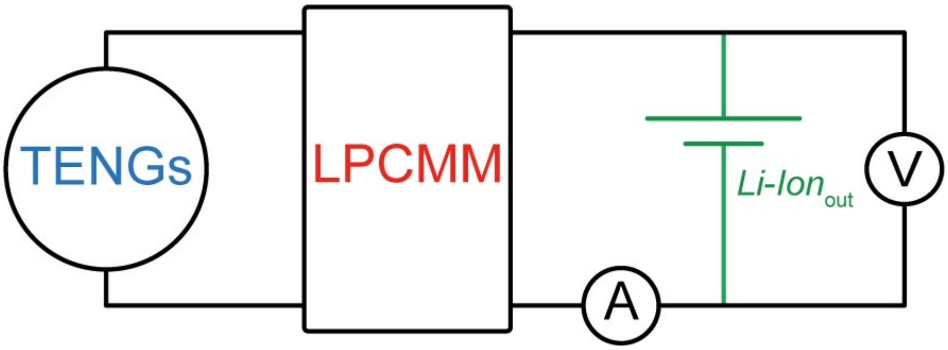

Fig. S23: Measurement circuit for lithium battery.

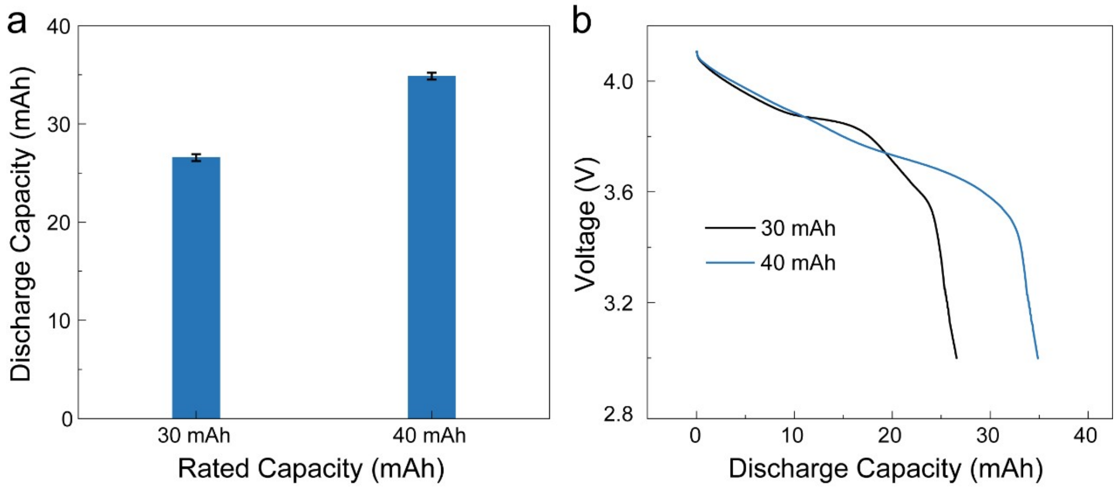

Fig. S24: Discharge capacities of lithium batteries with differing rated capacities. a. statistical data. b. curve data.

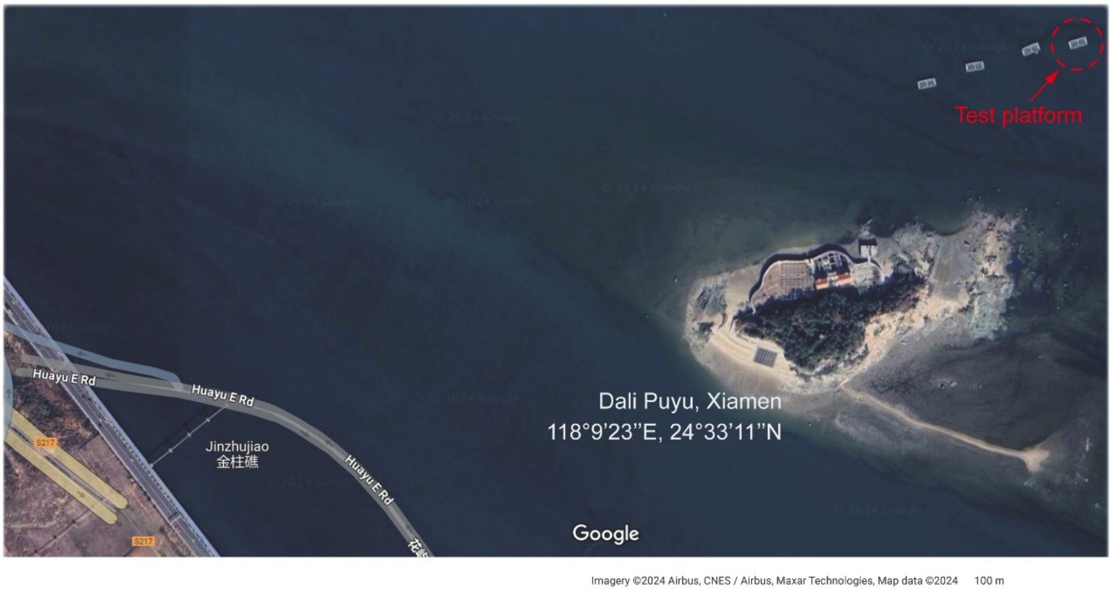

Fig. S25: Google maps for the test platform.

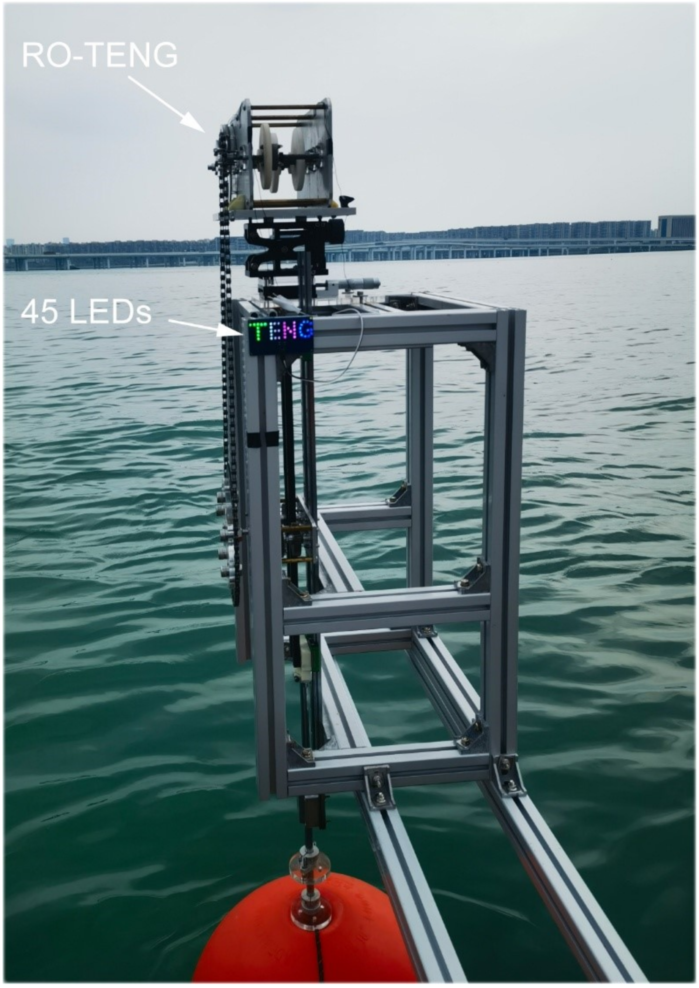

Fig. S26: Using the RO-TENG to light up 45 LEDs in the ocean environment.

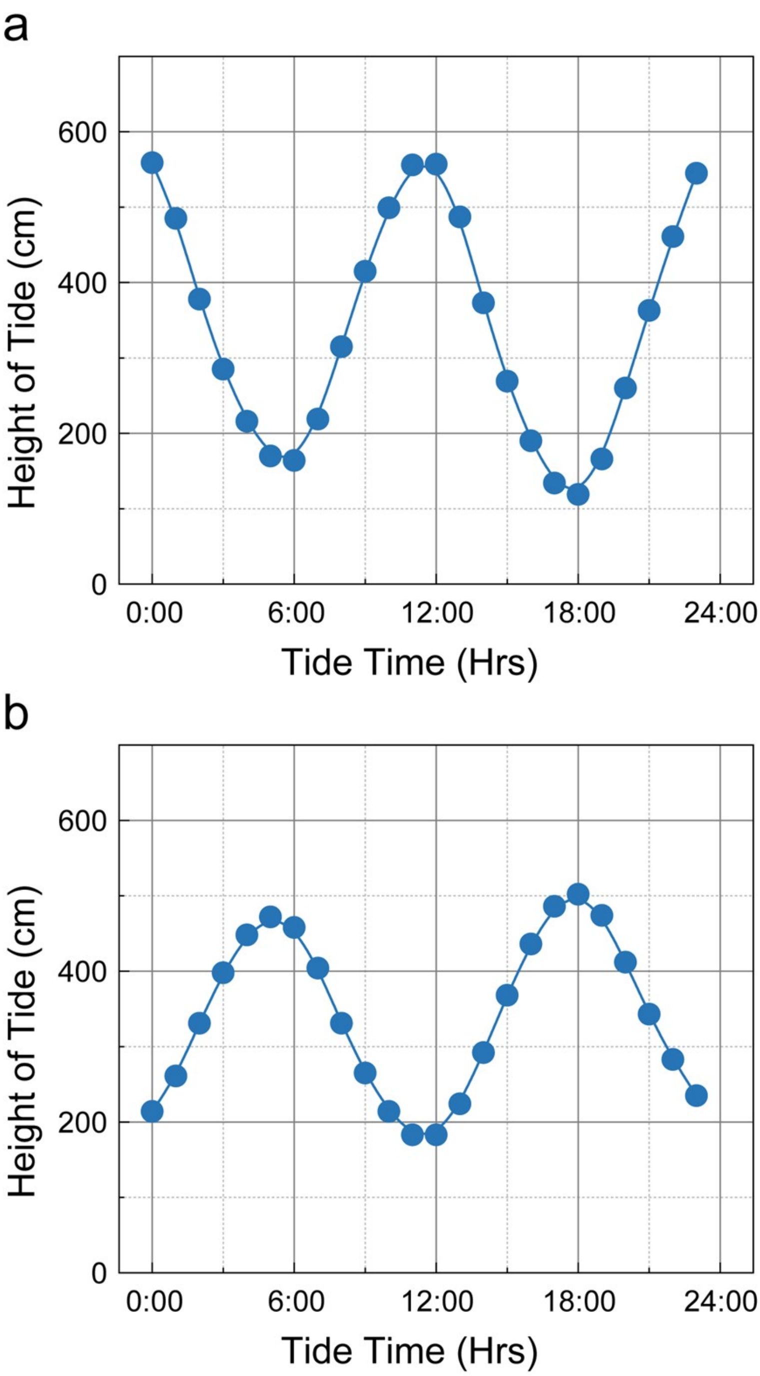

Fig. S27: The tidal data of Xiamen. a. October 9th. b. December 4th.The data from https://www.cnss.com.cn/html/tide.html

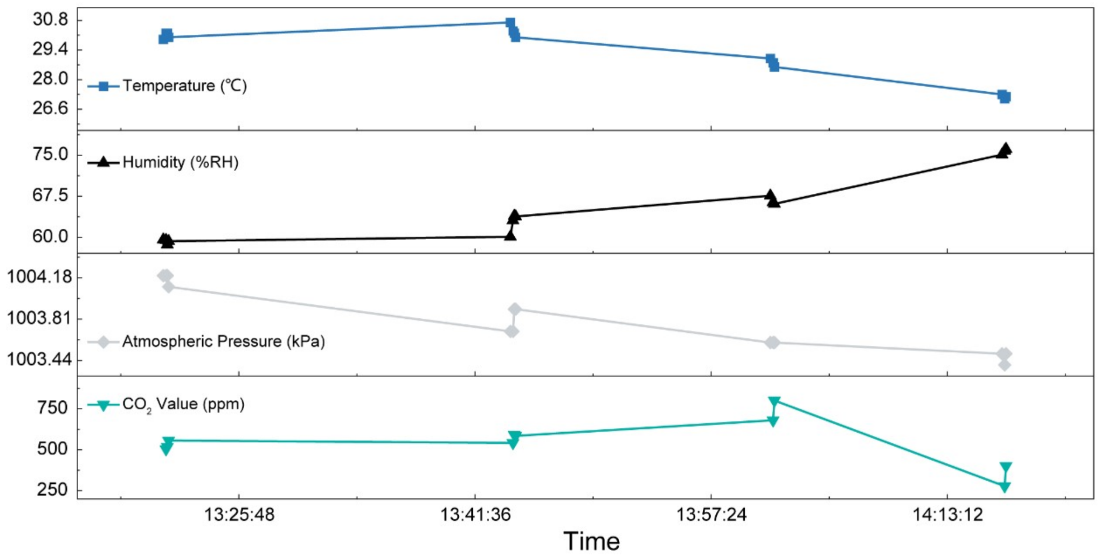

Fig. S28: Environmental data acquired from the monitoring system.

Supplementary Tables

Table S1: Comparison of main performance parameters of this work with those of previous research.

		Typical Output			
Ref.	**Year**	Current Characteristic	Optimal Resistance (MΩ)	Normalized Average Power Density ($W \cdot m^{-2} \cdot Hz^{-1}$)	Peak Power Density ($W \cdot m^{-2}$)
This work	2024	Periodic Attenuation	0.2	3.28±0.07	6.72±0.09
[29]	2024	Pulse Mode	2	0.5	N/A
[7]	2021	Periodic Attenuation	50	0.066	N/A
[32]	2023	Pulse Mode	N/A	0.101	N/A
[39]	2022	Periodic Attenuation	0.9	0.135	2.79
[2]	2024	Periodic Attenuation	5	0.426	0.65
[31]	2020	Pulse Mode	25	1.15	N/A
[17]	2020	Pulse Mode	0.3	0.051	N/A
[37]	2020	Pulse Mode	600	0.037	N/A
[36]	2021	Pulse Mode	35000	0.11	N/A
[18]	2023	Periodic Attenuation	0.56	0.027	0.1
[40]	2021	DC Type	60	0.271	N/A
[4]	2021	Periodic Attenuation	7	N/A	0.035
[12]	2021	Periodic	7	N/A	0.058

		Attenuation			
[9]	2021	Pulse Mode	10	N/A	4.08
[10]	2021	Periodic Attenuation	120	N/A	0.49
[5]	2024	Periodic Attenuation	200	N/A	0.016
[6]	2019	Pulse Mode	40	N/A	0.057
[30]	2020	Pulse Mode	5000	N/A	0.65
[21]	2022	Pulse Mode	20	N/A	0.34
[33]	2021	Periodic Attenuation	30	N/A	1.48

Table S2: Summarized parameters of the lithium battery.

30 mAh				
Size	9 mm, 9 mm, and 4.5 mm (Length, width, and height)			
Charging Limitations	Voltage	4.2 V	Current	0.5 C
Working Current	0.5 C			
Working Temperature	10℃-55℃			
Manufacturer	ZON.CELL, China			
40 mAh				
Size	16.5 mm, 9.5 mm, and 4.2 mm (Length, width, and height)			
Charging Limitations	Voltage	4.25 V	Current	0.5 C
Working Current	0.5 C			
Working Temperature	-20℃-60℃			
Manufacturer	Dajia Manyi Technology (Shenzhen) Co. Ltd., China			
80 mAh				
Size	22 mm, 11 mm, and 4.2 mm (Length, width, and height)			
Charging Limitations	Voltage	4.2 V	Current	0.5 C
Working Current	0.5 C			
Working Temperature	10℃-55℃			
Manufacturer	ZON.CELL, China			

Note: Photograph is shown in **Fig. S17**. The C-rate denotes the ratio between a battery's rated capacity and its charging or discharging current. For instance, if a battery has a rated capacity of 100 mAh, a C-rate of 1C indicates that the charging current for this battery is 100 mA during the constant current charging phase.

Table S3: Summarized component parameters of the transmitter and receiver.

Transmitter	
Main Chip	CC1310
Atmospheric Pressure Sensor	LPS22
Temperature and Humidity Sensor	SHT30
CO_2 Sensor	SCD41
Antenna	Rod (78.5 mm and 7.5 mm (height and diameter))
Receiver	
Main Chip	CC1310
UART Chip	CH340N
Antenna	Rod (78.5 mm and 7.5 mm (height and diameter))

Supplementary Notes

Note S1: The working principle of the RO-TENG integrated with a gearbox.

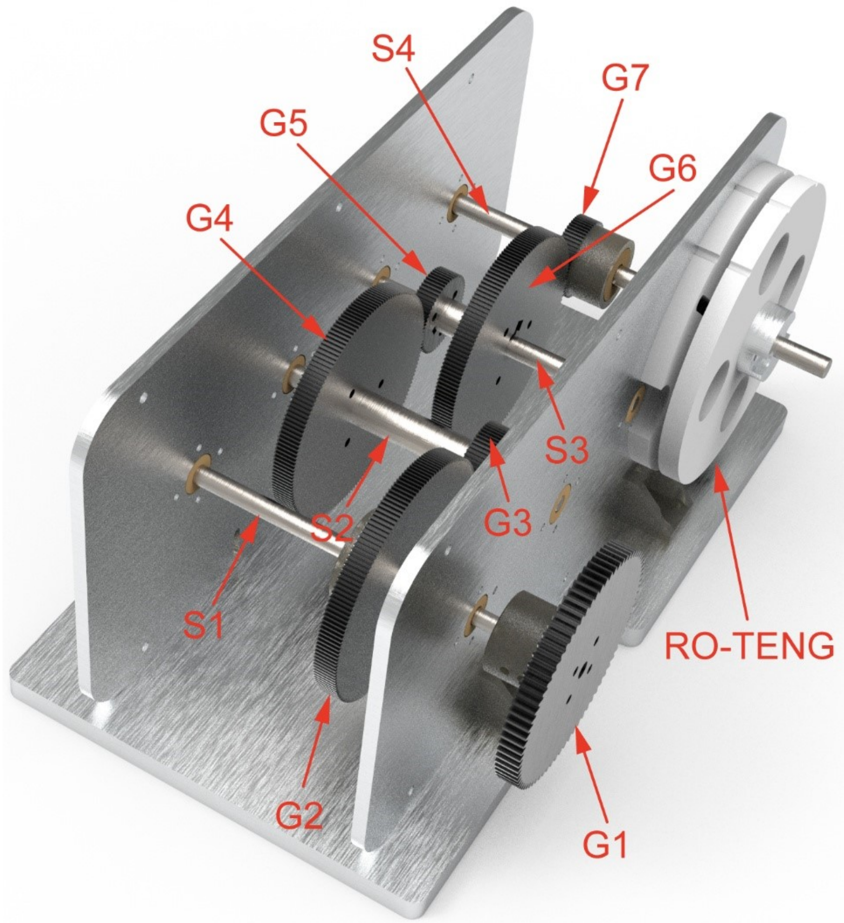

Fig. N1: Overall structure of the RO-TENG integrated with a gearbox

The motion transfer mechanism of the RO-TENG integrated with a gearbox is illustrated in **Fig. N1**. The power from the heaving motion of the wave drives the shaft S1 to rotate via the gear G1, and drives the gear pairs G2-G3 to rotate via the shaft S1 (The gear G2 is fixed to the shaft S1 by one-way bearing, which ensures that the gear G2 can only rotate in clockwise). The power is transmitted through shafts S2 and S3 to drive the gear pairs G4-G5 and G6-G7, which in turn rotate shaft S4 and subsequently the rotor of the RO-TENG. Since G7 is fixed to shaft S4 via a one-way bearing, a single excitation allows the rotor to continue rotating for a period of time before gradually coming to a stop. The parameters of the various gears are presented in Table N1.

Table N1: Summarized of the various gears.

Gear G1	
Modulus	1
Tooth number	80
Tooth thickness	10 mm
Pressure Angle	20°
Gear G2, Gear G4, Gear G6	
Modulus	0.5
Tooth number	170
Tooth thickness	10 mm
Pressure Angle	20°
Gear G3, Gear G5, Gear G7	
Modulus	0.5
Tooth number	60
Tooth thickness	10 mm
Pressure Angle	20°

Note S2: The mechanism of the UVLO.

The under-voltage lockout (UVLO) circuit consists of a hysteresis hysteretic comparison circuit and a DC-DC voltage regulator circuit. The hysteresis hysteretic comparison circuit, based on the operational amplifier, is a typical comparison circuit for detecting two threshold voltage (V_{th1} and V_{th2}) and outputting either a high or low level (**Fig. N2a**). It is characterized by hysteresis behavior, where the comparison circuit outputs a low level when V_C exceeds V_{th2}, and a high level when V_C falls below V_{th1}. Meanwhile, the circuit's output remains stable between these two thresholds (**Fig. N2b**). This also means that two threshold voltages can be used as the lithium battery operating voltage. In the lithium battery charging process, the circuit is utilized to detect the lithium battery voltage, and when the lithium battery voltage is less than V_{th2}, the postscript load circuit is disconnected. During the lithium battery charging process, the detection circuit is employed to monitor the lithium battery voltage. When the voltage drops below V_{th2}, the subsequent load circuit is disconnected. As the charging process continues and the voltage exceeds V_{th2}, the subsequent load circuit is activated, allowing the load to consume energy from the lithium battery. As energy is consumed, when the lithium battery voltage drops below V_{th2}, the back-loading circuit remains active due to the hysteresis characteristics of the circuit. The circuit remains on until the lithium battery voltage falls below V_{th1}, at which point the back-loading circuit is disconnected. Subsequently, the automatic control of the lithium battery's operating voltage range is achieved. The working voltage range for the lithium battery is set between 3.0 V-3.5 V.

Assuming that the resistive voltage dividing factor K:

$$K = R_5 / \left(R_4 + R_5\right)$$ * MERGEFORMAT (1)

Input voltage of op amp V_-: $V_- = V_C \times K$, when $V_C = 3V$, $V_- = 3 \times K$, when $V_C = 3.5V$, $V_- = 3.5 \times K$.

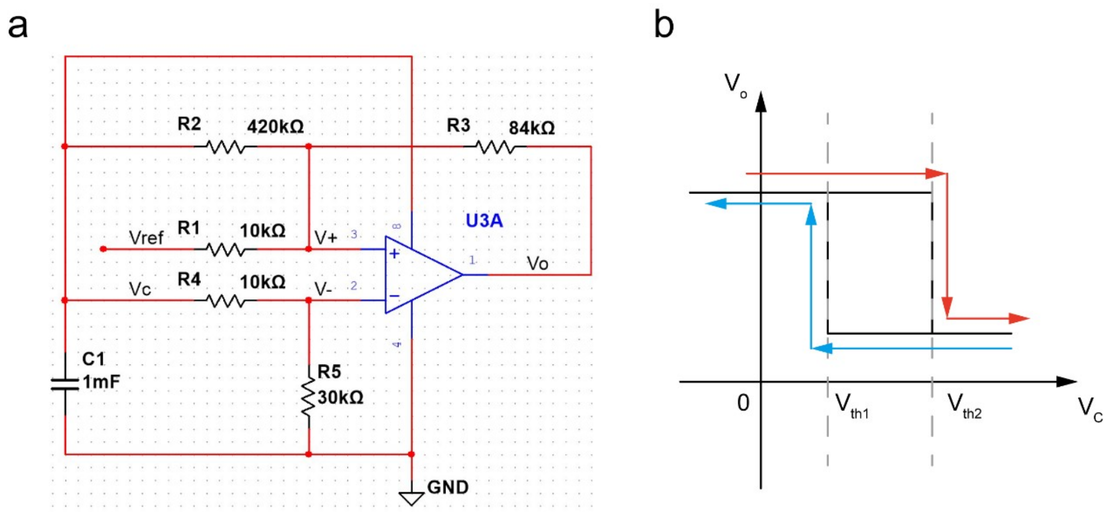

Fig. N2: a. Hysteresis comparison circuit scheme based on the operational amplifier. b. Characteristic of the hysteresis comparison circuit.

According to circuit requirements: $V_{th1} = 3 \times K, V_{th2} = 3.5 \times K$

The circuit is a positive feedback circuit, when $V_+ > V_-$, V_O output high voltage, when $V_+ < V_-$, V_O output low voltage. When the output of high voltage circuit V_O ($V_O \approx V_C = 3.5V$), according to Kirchhoff's law:

$$\left(V_{ref} - V_+\right)/ R_1 + \left(V_C - V_+\right)/ R_2 + \left(V_O - V_+\right)/ R_3 = 0 \qquad \backslash *$$

MERGEFORMAT (2)

When V_- is increasing ($V_+ < V_-$), V_O will output a low voltage, depending on the virtual short of the op amp ($V_+ = V_- = 3.5 \times K$), bring in the equation* MERGEFORMAT (2):

$$\left(V_{ref} - 3.5 \times K\right)/ R_1 + \left(3.5 - 3.5 \times K\right)/ R_2 + \left(3.5 - 3.5 \times K\right)/ R_3 = 0 \qquad \backslash *$$

MERGEFORMAT (3)

a b

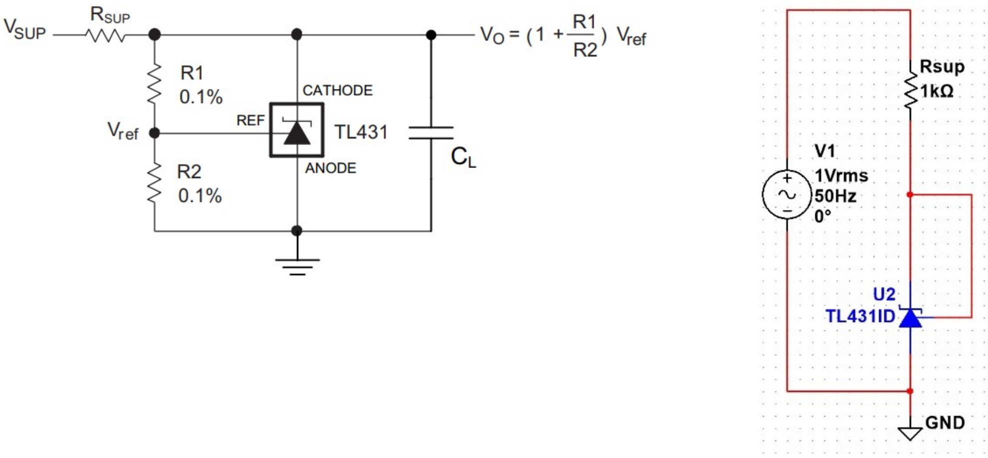

Fig. N3: a. Typical circuit of the TL341. b. Simulation circuit of the V_{ref} based on the TL341.

When the circuit V_O output low voltage ($V_O \approx 0 = 3V$), according to Kirchhoff's law:

$$\left(V_{ref} - V_+\right)/ R_3 + \left(V_C - V_+\right)/ R_4 + \left(V_O - V_+\right)/ R_5 = 0$$ * MERGEFORMAT (4)

When V_- is increasing ($V_+ > V_-$), V_O will output a high voltage, depending on the virtual short of the op amp ($V_+ = V_- = 3 \times K$), bring in the equation* MERGEFORMAT (4):

$$\left(V_{ref} - 3\times K\right)/ R_1 + \left(3 - 3\times K\right)/ R_2 + \left(-3\times K\right)/ R_3 = 0$$ * MERGEFORMAT (5)

According to the working voltage range of 2.5 V to 4 V for the lithium battery, we selected V_{ref} as the lowest voltage, 2.5 V. This circuit is selected as the reference voltage regulator chip TL431 (**Fig. N3a**), according to the chip manual, its reference voltage is calculated as equation* MERGEFORMAT (6).

$$V_O = \left(1 + \frac{R_1}{R_2}\right) V_{ref}$$ * MERGEFORMAT (6)

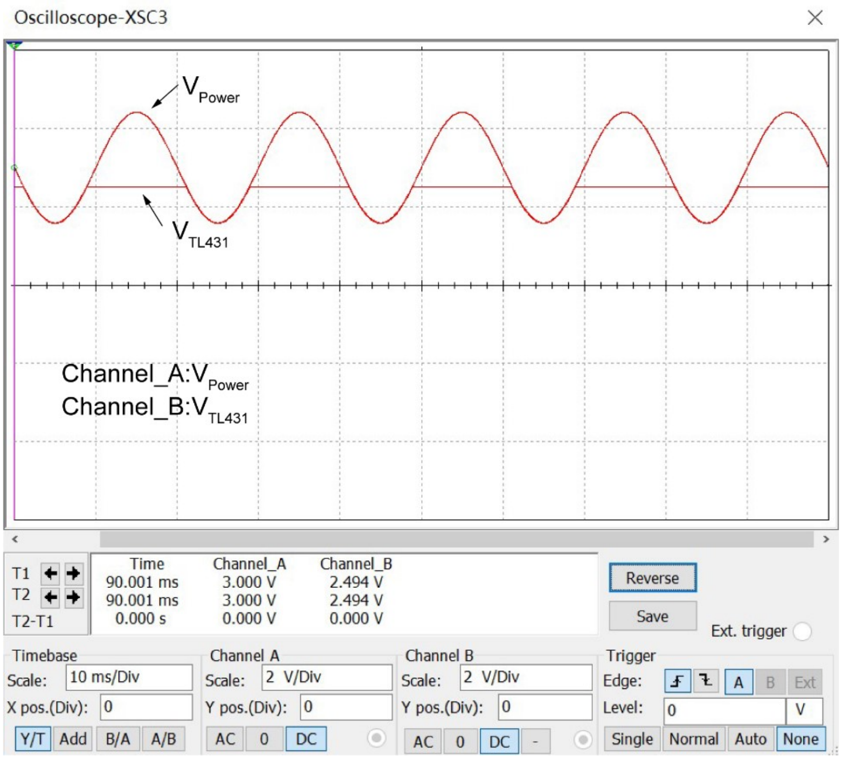

Fig. N4: Simulation data of the V_{ref} .

When R1=0, the equation* MERGEFORMAT (6) can be expressed by $V_O = (1 + 0 / R_2) \times 2.5 = 2.5V$, R_{SUP} is taken as 1 kΩ. The Simulation circuit and data of the V_{ref} based on the TL341 are shown in **Fig. N3b** and **Fig. N4**, respectively. When the input voltage is greater than 2.5 V, its output voltage 2.5 V, when the input voltage is less than 2.5 V, its output voltage is the input voltage.

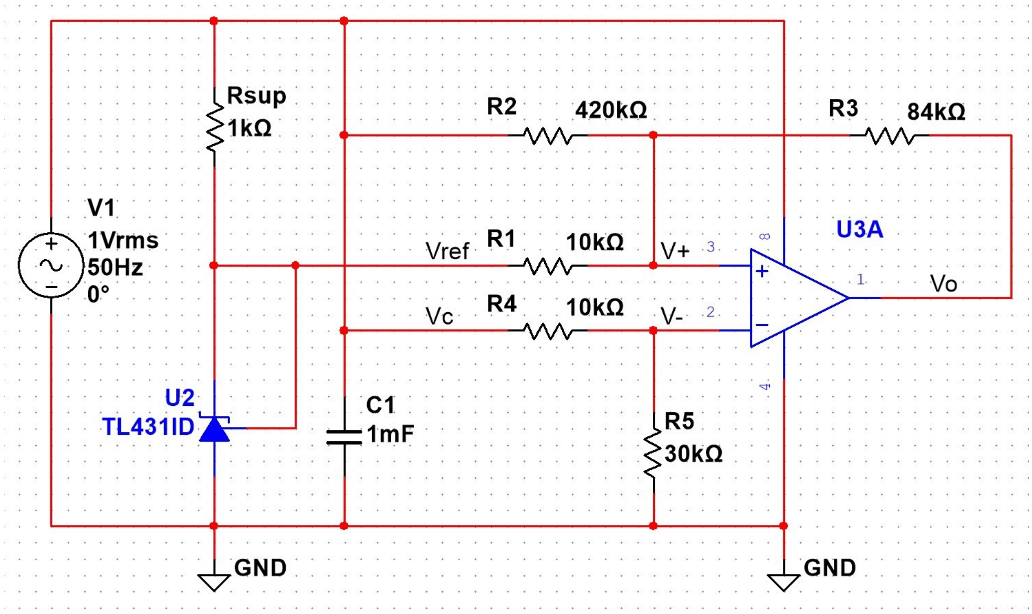

Fig. N5: Simulation circuit of the hysteresis comparison circuit.

When $Vref = 2.5V$, equation * MERGEFORMAT (3) and * MERGEFORMAT (5) can be expressed as:

$$(2.5-3.5\times K)/R_1+(3.5-3.5\times K)/R_2+(3.5-3.5\times K)/R_3=0$$ * MERGEFORMAT (7)

$$(2.5-3\times K)/R_1+(3-3\times K)/R_2+(-3\times K)/R_3=0$$ * MERGEFORMAT (8)

According to equation * MERGEFORMAT (1), assuming K=3/4, R_1=10 kΩ, R_4=10 kΩ, the following values are obtained: R_5=30 kΩ, R_2=420 kΩ, R_3=84 kΩ. The simulation circuit and data for the hysteresis comparator are presented in **Fig. N5** and **Fig. N6**, respectively. From the simulation results, it can be observed that when the voltage (V_{Power}) exceeds 3.506 V, a low voltage (V_{Out}) is output. Conversely, when the V_{Power} drops below 3.010 V, the V_{Out} is output. These findings satisfy the design requirements. Meanwhile, based on the output characteristics of the hysteresis circuit, a phase inverter should be used to drive the NMOS in order to control the back-end circuit. The overall circuit configuration is illustrated in **Fig. N7**. The load resistor is replaced by a 1 kΩ resistor (R_7), and the voltage across its terminals corresponds to the voltage across the load terminals. The simulation data for the UVLO is presented **Fig. N8**. From the **Fig. N8**, it can be observed that when the voltage (V_C) exceeds 3.506 V, the voltage across the R_7 resistor (V_{Out}) is equal to V_C. Conversely, when the V_C drops below 3.010 V, the V_{Out} is 0 V. These findings satisfy the design requirements.

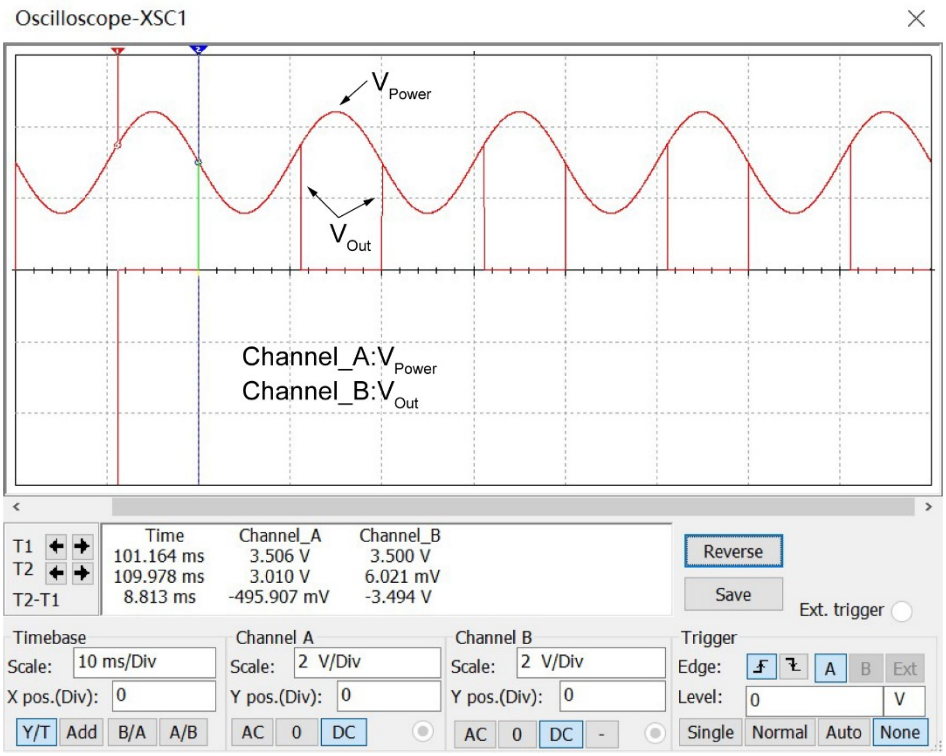

Fig. N6: Simulation data of the hysteresis comparison circuit.

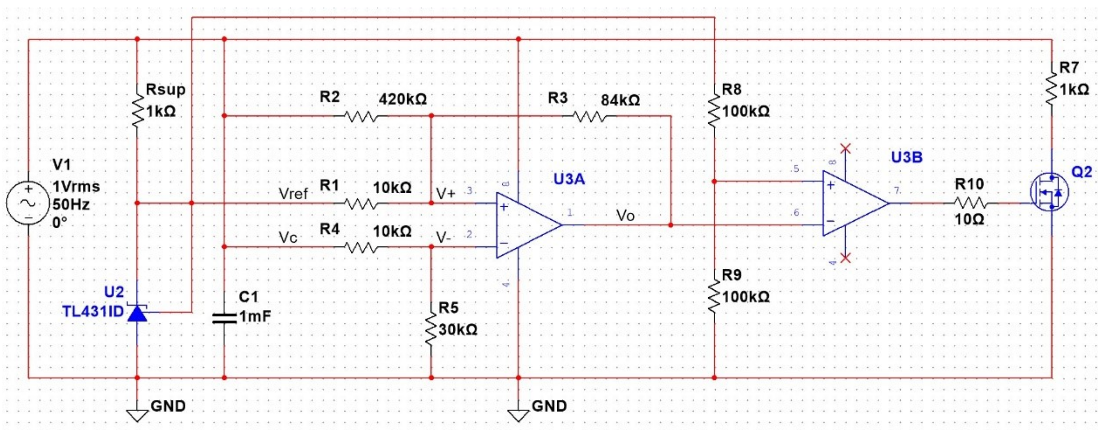

Fig. N7: Simulation circuit of the UVLO.

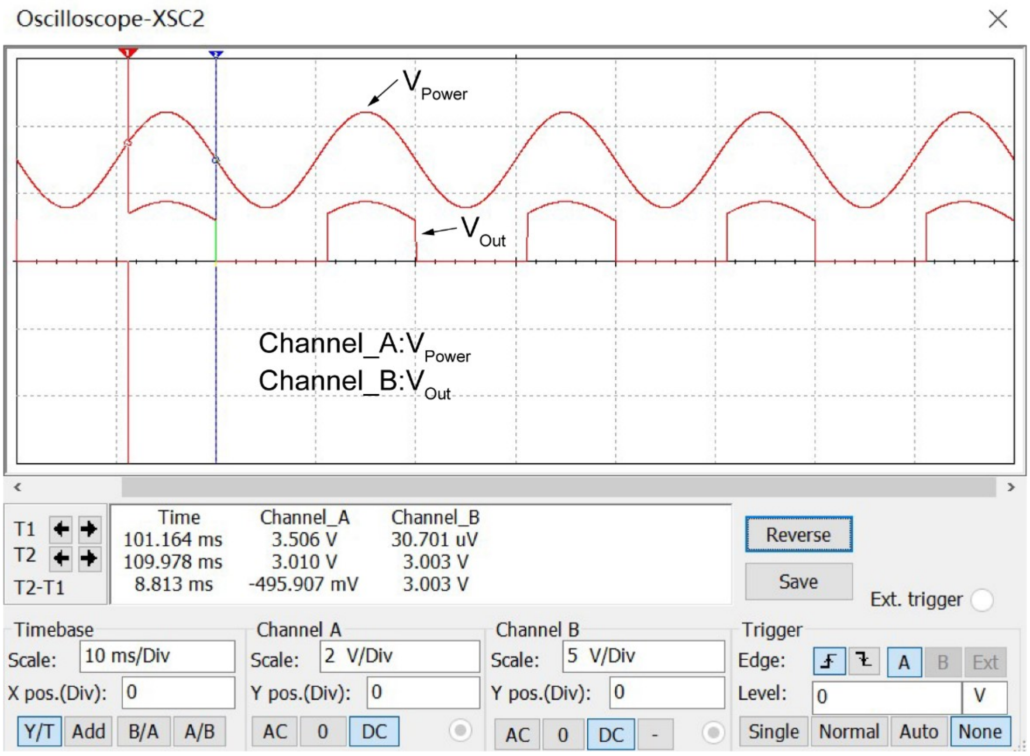

Fig. N8: Simulation data of the UVLO.

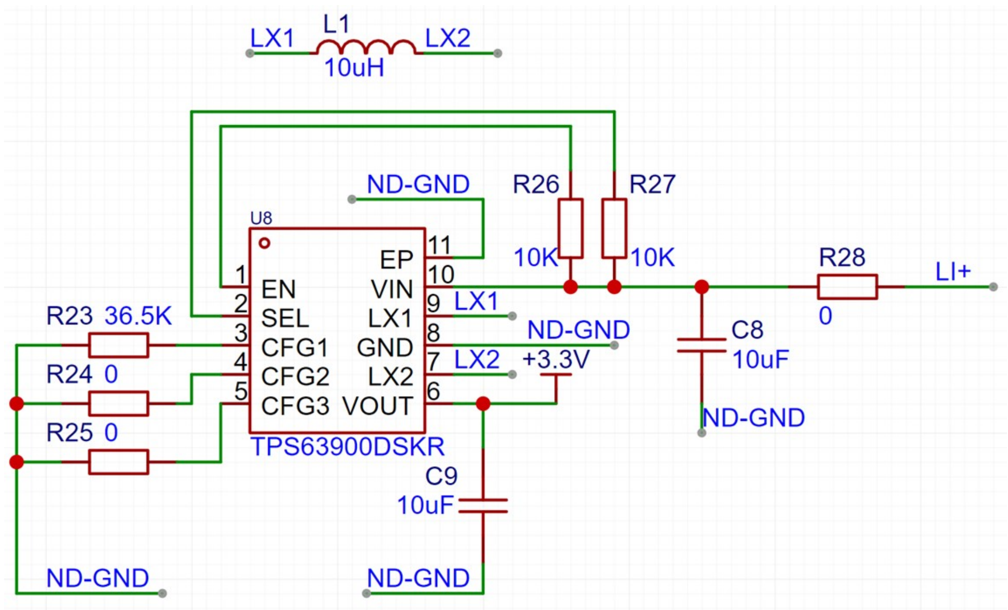

Fig. N9: Schematic circuit of the TPS63900DSKP.

On the other hand, to ensure that the load receives a stable voltage throughout the operating range of the lithium battery, a low-power DC-DC power supply chip is employed. The application circuit for this chip is illustrated in **Fig. N9**. The chip is capable of stabilizing the output at 3.3 V when the input voltage ranges from 3.0 V-3.5 V. The measured data for the UVLO integrated with a DC-DC chip are presented in **Fig. N10**. As illustrated in the **Fig. N10**, a stabilized output voltage of 3.3 V is maintained when the input voltage exceeds 3.56 V. Conversely, when the input voltage drops below 3.04 V, the output voltage is 0 V.

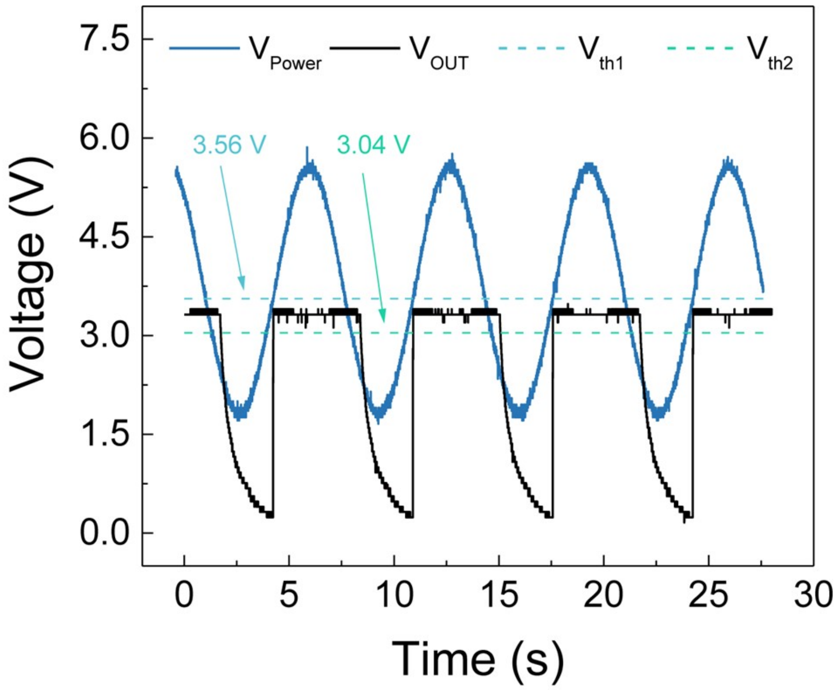

Fig. N10: Measured data of the UVLO integrated with a DC-DC chip.

Supplementary Movies

Movie S1: A 4x5 wireless Bluetooth sensors array is driven by the RO-TENG with LPCMM.

Movie S2: Self-powered sensing system powered by the RO-TENG under high-frequency wave conditions.

Movie S3: Self-powered sensing system powered by the RO-TENG under low-frequency wave conditions.

Movie S4: Lighting up LEDs by the RO-TENG in the ocean environment.

Movie S5: Receiver #1 data in the real ocean environment.

Movie S6: Receiver #2 data in the real ocean environment.

References

S1. Z. Lin, B. Zhang, H. Zou, Z. Wu, H. Guo, Y. Zhang, J. Yang and Z. L. Wang, *Nano Energy*, 2020, **68**, 104378.

S2. P. Chen, J. An, S. Shu, R. Cheng, J. Nie, T. Jiang and Z. L. Wang, *Adv. Energy Mater.*, 2021, **11**, 2003066.

S3. Y. Luo, P. Chen, L. N. Y. Cao, Z. Xu, Y. Wu, G. He, T. Jiang and Z. L. Wang, *Adv. Funct. Mater.*, 2022, **32**, 2205710.

S4. Y. Liu, W. Yan, J. Han, B. Chen and Z. L. Wang, *Adv. Funct. Mater.*, 2022, **32**, 2202964.

S5. M. Liu, X. Zhang, Y. Xin, D. Guo, G. Hu, Y. Ma, B. Yu, T. Huang, C. Ji, M. Zhu and H. Yu, *Adv. Sci.*, 2024, **11**, 2401636.

S6. D. Liu, L. Zhou, Y. Gao, D. Liu, W. Qiao, J. Shi, X. Liu, Z. Zhao, Z. L. Wang and J. Wang, *Adv. Energy Mater.*, 2024, **14**, 2401958.

S7. L. He, C. Zhang, B. Zhang, O. Yang, W. Yuan, L. Zhou, Z. Zhao, Z. Wu, J. Wang and Z. L. Wang, *ACS Nano*, 2022, **16**, 6244-6254.

S8. P. Chen, Y. Luo, R. Cheng, S. Shu, J. An, A. Berbille, T. Jiang and Z. L. Wang, *Adv. Energy Mater.*, 2022, **12**, 2201813.